Photoexcited single metal atom catalysts for heterogeneous photocatalytic H_2O_2 production: Pragmatic guidelines for predicting charge separation

Zhenyuan Teng[a,d,1], Wenan Cai[a,1], Wenwen Sim[a], Qitao Zhang[b,*], Chenyin Wang[c,d], Chenliang Su[b], Teruhisa Ohno[a,d,*]

[a]*Department of Applied Chemistry, Faculty of Engineering, Kyushu Institute of Technology, Kitakyushu 804-8550, Japan*

[b]*International Collaborative Laboratory of 2D Materials for Optoelectronics Science and Technology of Ministry of Education, Institute of Microscale Optoelectronics, Shenzhen University, Shenzhen 518060, China*

[c]*College of Chemistry and Chemical Engineering, Jiangsu Key Laboratory of Environmental Engineering and Monitoring, Yangzhou University, 180 Si-Wang-Ting Road, Yangzhou 225002, China*

[d]*Joint Laboratory of Yangzhou University, Kyushu Institute of Technology, Yangzhou University, 180 Si-Wang-Ting Road, Yangzhou 225002, China*

[1]*These authors contributed equally*.

Abstract

A systematic investigation of electronic configuration and excitation properties is extremely urgent for establishing a guideline to boost H_2O_2 production with metal single-atom photocatalysts (M-SAPCs). Herein, a series of metal-ion incorporated M-SAPCs was prepared, isolating of three transition metals (Fe, Co, Ni) and two main-group metals (In, Sn) single site by pyridinic N atoms in polymeric carbon nitride (PCN) skeleton. The models in which metal ions are isolated by non-defected g-C_3N_4 units (Melem_3M) are consistent with the practically prepared M-SAPC in terms of band structures and electronic configurations. Transition density and molecular orbital analysis revealed that the atomically dispersed In (III) and Sn (IV) significantly improve the charge separation with an ideal electronic configuration for the end-on adsorption of oxygen for a boosted $2e^-$. The experimental charge separation properties and photocatalytic activities of M-SAPC showed good accordance with the computed charge transfer profiles of Melem_3M, manifesting the rationalities and validities of as-proposed guidelines.

Keywords: Photocatalysis, oxygen reduction reaction, H_2O_2 production, single-atom catalyst, time-dependent density functional theory

1. Introduction

H_2O_2 is used as an industrially crucial oxidant and is a promising future solar fuel with higher energy (60 wt.% H_2O_2, 3.0 MJL^{-1}) density than compressed H_2 gas (35 MPa, 2.8 MJL^{-1}) [1-4]. H_2O_2 is currently produced by an energy-consuming, waste-intensive, and indirect anthraquinone method [5, 6]. Photocatalytic H_2O_2 production on semiconductor materials from water and oxygen has emerged as a promising safe, environmental-friendly and energy-efficient process [7-9]. To achieve a high selectivity and rate for H_2O_2 production, it is necessary to boost the $2e^-$ oxygen reduction reaction (ORR) [10] (eq. 1) or $2e^-$ water oxidation reaction (WOR) (eq. 2) [11]. A photocatalytic $2e^-$ WOR pathway is quite difficult to achieve because the as-synthesized H_2O_2 will decompose at the high oxidative potential (1.76 V vs. NHE) [11, 12]. Alternatively, solar H_2O_2 can be obtained from an ORR via a $2e^-$ pathway [9, 10, 13-17]. Various photocatalysts such as inorganic ZnO, TiO_2, and CdS and organic graphitic carbon nitride (g-C_3N_4) have been found to be active for the artificial photosynthesis of H_2O_2 in a particulate system [10, 18-20]. Nevertheless, the activity achieved is limited to a low level due to (1) low selectivity for the $2e^-$ process and (2) the low charge separation of photocatalysts.

$$O_2+2H^++2e^-\rightarrow H_2O_2 \quad (0.695\ V\ vs.\ NHE) \tag{1}$$

$$2H_2O+2h^+\rightarrow H_2O_2+2H^+ \quad (1.76\ V\ vs.\ NHE) \tag{2}$$

$$O_2+4H^++4e^-\rightarrow 2H_2O \quad (1.23\ V\ vs.\ NHE) \tag{3}$$

Tuning metallic sites into catalytic centers can boost both the activity and selectivity of ORR [21]. $4e^-$ ORR and $2e^-$ ORR are two competitive reactions in electrochemical systems that strongly depend on the type of O_2 adsorption [21]. O_2 adsorption on a metal surface can be generally classified into three types (Scheme 1A): one end-on type (Pauling-type), two side-on types (Griffiths-type and Yeager-type) [21, 22]. Side-on adsorption of O_2 is used to split O-O bond, which may result high selectivity for $4e^-$ ORR, while the end-on O_2 adsorption can minimize the O-O bond breaking, leading to a suppressed $4e^-$ ORR (eq. 3) and thus a highly selective $2e^-$ ORR [23]. Both end-on and side-on types of O_2 molecular adsorption occur on the surfaces of metal particles, and thus the O-O bond splitting on the surface of metal particles is therefore difficult to prevent [21-23]. On the other hand, the

adsorption of O_2 molecule on atomically isolated sites is usually end-on type (Scheme 1B), which therefore could reduce the possibility of O-O bond breaking [24-26]. For instance, supported single-atom catalysts (SACs) with Pt^{2+} [27, 28] and Co-N_4 [29, 30] centers can electrochemically reduce O_2 to H_2O_2 via a $2e^-$ ORR pathway with ultrahigh selectivity (>96%). Many theoretical investigations have also revealed the nature of ORR selectivity to predict favorable reaction pathways for $2e^-$ ORR using a computational hydrogen electrode (CHE) model [31]. However, these SACs and the CHE models is difficult to be directly used in the case of photocatalytic systems since the charge separation properties are not the dominant factor to influence electrochemical activity but a crucial factor to affect the photocatalytic activity [32, 33]. For instance, transition metals (TMs) with the half-filled d electrons, i. e., Mn, Fe, Co, Ni and Cu, usually show high activities if these elements are used to construct efficient electrocatalysts [29, 30, 34], while these elements usually show low photocatalytic activities because of the charge recombination occurred at these metallic sites [35]. Main-group metals with a d^{10} electronic configuration can eliminate the formation of an intermediate band in the band structure and usually show good activities in many artificial photosynthesis systems [36]. A systematic investigation of electronic configuration and excitation properties of isolated main-group metal and TM sites could provide a comprehensive understanding between theoretical design to practical activities.

Here Scheme 1

To this end, a series of metal ion-incorporated single atom photocatalysts (M-SAPCs) was prepared by a facile wet-chemical method combined with the thermal condensation treatment by isolation of TM metals (Fe, Co, Ni) and main-group (In, Sn) sites with a nitrogen-rich polymeric carbon nitride skeleton. The chemical states of the metal element and the band positions of the catalyst were firstly investigated. Based on the experimental data, we then constructed and validated cluster models that can represent the electronic structure of as-prepared SAPCs. The nature of excited states (ES) was clarified in these models to obtain a comprehensive understanding of possible charge separation properties of M-SAPCs for the first time by employing the time-dependent density functional theory (TDDFT). Verified by the experimental results of photoluminescence (PL), light-driven

electrochemical impedance spectroscopy (EIS) and photocurrent response profiles, a theoretical guideline based on the validated electronic configuration and excitation properties has been established. This guideline provides a blueprint for the design of an efficient single-atom photocatalyst at atomic levels.

2. Experimental details

2.1 Preparation of single metallic atom photocatalysts

The purities of all reagents for preparation of photocatalysts and for photoelectrochemical measurements were above analytical grade unless otherwise stated. Pristine polymeric carbon nitride (PCN) was prepared by calcination of 4 g dicyandiamide at 560 °C in N_2 for 4 h. Typically, $FeCl_3 \cdot 6H_2O$ (Wako Pure Chemical Industries, Ltd.), $CoCl_2 \cdot 6H_2O$ (Wako Pure Chemical Industries, Ltd.), $NiCl_2 \cdot 6H_2O$ (Wako Pure Chemical Industries, Ltd.), $InCl_3 \cdot 4H_2O$ (Wako Pure Chemical Industries, Ltd.) and $SnCl_4 \cdot 5H_2O$ (SIGMA-ALDRICH, Co., Ltd.) were used as metallic sources for the formation of metal catalytic sites. First, 1 mmol metal chloride were dissolved into ethanol solution with sonification treatment for 60 min. Then, 4 g dicyandiamide was dispersed into solution by sonification for another 60 min. After that, the solution was removed by a vacuum evaporator, and the as-obtained powders were dried in a vacuum oven at 60 °C for 4 h. The metal ion-dispersed M-SAPCs were prepared by calcinating the obtained mixture at 560 °C in N_2 for 4 h (Figure S1A). The as-prepared M-SAPCs were named according to the incorporated metal species, i. e., Fe-SAPC, Co-SAPC, Ni-SAPC, In-SAPC and Sn-SAPC. The as-prepared sample were all washed in the 2% (v/v) HCl at 80 °C for 24 h to remove the unfixed metal species such as nanoparticles [29].

2.2 Material characterization

High-resolution transmission electron microscopy (HRTEM), high-angle annular dark field scanning transmission electron microscopy (HAADF-STEM) and energy-dispersive X-ray spectroscopy (EDS) were performed using a Titan Cubed Themis G2 300 electron microscope (Field Electron and Ion Company, USA) with an accelerating voltage of 300 kV.

The crystalline phases were characterized by a powder X−ray diffraction (XRD) instrument (MiniFlex II, Rigaku Co.) with CuKα (λ = 1.5418 Å) radiation (cathode voltage: 30 kV, current: 15 mA). X−ray photoelectron spectroscopy (XPS) measurements were performed using an ESCALAB 250Xi (Thermo Scientific, USA). The binding energy was calibrated by taking the carbon (C) 1s peak of adventitious carbon at 284.6 eV. UV-vis diffuse reflectance spectroscopy (UV-DRS) was performed using a UV/VIS/NIR spectrometer (UV-2600, Shimadzu Co.). Photoluminescence spectroscopy was acquired using a FP-8500 spectrofluorometer (JASCO Corporation, Japan).

2.3 Computational methods

To analyze the excited states of pristine PCN and PCN coordinated with single metal ions, the Gaussian09 program S2 within TDDFT was used [37]. All optimization and frequency simulations were carried out by utilizing wb97xd/6-311 G(d) level of theory for C, N and H elements and SDD for metal elements [9]. PCN synthesized by thermal polymerization usually contains several defects and shows a poor crystallinity with a short range order of the lattice [38, 39]. In this case, the single metal atom-dispersed catalysts are simulated using three cluster models, which the M atom is bound with the skeleton. The melem_3M represents a single metallic ion coordinated by non-defected PCN unit, i.e., *graphitic carbon nitride (g-C_3N_4) unit*. The melem_4MS and melem_4MC are used to simulate two possible geometry configurations of metal ions coordinated by a defected PCN unit, i. e., *melon unit*. Based on the influence of ionizable groups on the isoelectric points of carbon-based materials previously reported [40, 41], the incorporated metal ions show positive charges in nature. In this case, the charges for cluster models are set to be the same as the chemical states which are confirmed by XPS measurements. The stability of SACs is evaluated by calculating the formation energy [29], which is defined as:

$$E_{form} = E_{Melem\_xM} - E_{Melem\_x} - E_M,$$

where E_{Melem_xM}, E_{Melem_x}, and E_M represent the energies of metal ion coordinated by PCN, pristine PCN, and metallic ions.

Multiwfn Ver. 3.6 (released on May 21, 2019) was used for analysis of the excitation

and charge transfer properties [42]. The charge transfer (CT) length in the Cassian coordinates (X/Y/Z) could be measured by the distance between the centroid of hole and electron in the corresponding directions (denoted as *D* index) [37, 42]. Furthermore, Coulomb attraction between hole and electron (exciton binding energy) was also computed for estimation of charge recombination properties [43, 44].

Visualization of holes, electrons and transition density was also performed by Multiwfn: functions of *IOp(9/40=3)* were set during the vertical excitation based on TD-DFT calculation [42]. The electron distributions at these excited states were presented as heatmaps by using the combination of GaussView 5.0 and Multiwfn. The iso-surface of LUMO orbitals was presented by setting the isovalue to 0.05.

2.4 Activity measurements

Each catalyst (50 mg) was added to 10% ethanol solution (3 mL ethanol with 27 mL deionized water) in a borosilicate glass bottle (φ 45 mm; capacity, 50 mL), and the bottle was sealed with a rubber septum cap. The catalyst was dispersed well by ultrasonication for 15 min, and O_2 was bubbled through the solution for 30 min. The bottle was immersed in a temperature-controlled air bath at 298 ± 0.5 K with wind flowing and was photo-irradiated at λ > 420 nm using a 500 W Xe lamp (PXE-500, USHIO Inc.) with magnetic stirring. The amount of H_2O_2 was determined by a colorimetric method using PACKTEST (WAK-H_2O_2, KYORITSU CHEMICAL-CHECK Lab., Corp.) equipped with a digital PACKTEST spectrometer (ED723, GL Sciences Inc.).

3. Results and discussion

3.1 Characterization of M-SAPCs

The crystalline structures of M-SAPCs were firstly investigated by XRD measurements (Figure S1B). XRD patterns of all M-SAPC samples showed two characterization peaks at about 27.4° and 13.1°, ascribing to the interlayer stacking {002} and the inner planar structure packing {100} of tri-s-triazine units, respectively. The slight shift in the diffraction pattern of the {002} lattice compared with the XRD pattern of pristine PCN (27.6°) can be

attributed to the electrostatic repulsion between interlayers when positive ions were incorporated into the PCN matrix [9]. Although the peak intensities of the {002} lattice slightly changed after the introduction of heterometal ions, there was almost no change in the peak intensity of the {100} lattice, indicating that the incorporation of metal species has almost no influence on the in-plane structure of tri-s-triazine [20]. As a powerful tool for discerning individual heavy atoms, high-angle annular dark-field scanning transmission electron microscopy (HAADF-STEM) was used to further confirm the morphology and elemental distribution and configuration of metal species. The morphologies of pristine PCN (Figure 1A) and all M-SAPCs were bulk materials with a homogeneous distribution of metal elements as shown in the HAADF-STEM mapping images with low magnification (Figure S2). After aberration-correction TEM measurement in high magnification, Figure 2B-F show that the bright spots with high density corresponding to metallic atoms are uniformly dispersed in the carbon nitride matrix. The size distribution inserted in Figure 2B-F reveals that the size of 99.6% of the metallic species is less than 0.2 nm, manifesting that incorporated metal exists exclusively as atomically dispersed single atoms [45]. The weight percentages of the metal species in the as-prepared M-SAPCs are all less than 1% (Table S1) with a similar amount of metal atom in a certain mass of catalyst (about 0.5~0.6 mmol per 1 g catalyst). Note that metal nanoparticles could remain on the surface of M-SAPC (taking In-SAPC as an example) if the as-prepared photocatalyst did not undergo the acid washing process (Figure S3).

Here is Figure 1.

To further reveal the interaction between the isolated metallic sites and the PCN skeleton, chemical states of pristine PCN and M-SAPCs were investigated by XPS measurements. The ratio obtained by dividing the integration area of the C 1s peak by the integration area of N 1s was almost constant in the XPS survey spectra of pristine PCN and M-SAPC (Figure 2G), further indicating that incorporation of isolated metallic ion sites has almost no influence on the skeleton of PCN matrix. As shown in the high-resolution C 1*s* spectra of pristine PCN and M-SAPC (Figure S4), the typical components around 288.1 eV and 284.6 eV (indexed as N–C=N and adventitious carbon, respectively) are almost

the same, whereas no new peak appeared in C 1s spectra. These results revealed that the chemical state of surface carbon remained almost the same, indicating that the carbon atoms hardly interact with metallic ions. Three peaks at 401.0 eV, 399.8 eV and 398.7 eV can be assigned to -NH_2, tertiary nitrogen, and C=N-C bonds, respectively. It is notable that nitrogen peak (N 1s) appears around 398.3 eV in the spectra of M-SAPC, which could be assigned to the chemical composition of N-Metal (Figure 2H) [46]. High-resolution Cl 2p spectra (Figure S5) confirmed that all fluoride elements were completely removed, excluding the possibility of chemical states of M-Cl. The spectra of Fe 2p can be deconvoluted to six peaks at 728.0 eV, 724.0 eV, 722.0 eV, 715.2 eV, 711.2 eV and 709.2 eV (Figure S6A), which could be respectively assigned to the satellite peak of Fe $2p_{1/2}$, Fe^{3+}-N $2p_{1/2}$, Fe^{2+}-N $2p_{1/2}$, satellite peak of Fe $2p_{3/2}$, Fe^{3+}-N $2p_{3/2}$ and Fe^{2+}-N $2p_{3/2}$, which is close to the binding energy of Fe_2O_3 and FeO. These results revealed that that the chemical states of Fe is mixed with (II) and (III). Similarly, referring to the chemical states of CoO, NiO, In_2O_3 and SnO_2, the chemical states of atomically dispersed Co, Ni, In and Sn species in the as-prepared M-SAPC are close to (II), (II), (III) and (IV) (Figure S6B-E), respectively [46].

Here is Figure 2.

To investigate the bandgap width, CBM and VBM of the as-prepared M-SAPC samples, UV-vis DRS, Mott-Schottky and VB-XPS measurements were respectively conducted. As shown in Figure 2A, the light absorption edge of pristine PCN (445 nm) is smaller than that of M-SAPCs (> 450 nm), indicating that the incorporation of metal ions narrowed the band gap. The band gap width followed a sequence of $E_{gIn\text{-}SAPC} > E_{gNi\text{-}SAPC} \approx E_{gCo\text{-}SAPC} > E_{gSn\text{-}SAPC} > E_{gFe\text{-}SAPC}$. The VBM of M-SAPCs remained almost constant to be 1.46 eV as shown in the VB-XPS results (Figure S7). As shown in Mott-Schottky plots (Figure S8), the CBM of M-SAPC samples gradually became more positive from -1.28 eV for pristine PCN to -1.00 eV for M-SAPCs (Figure S8). Based on as-obtained bandgap width and band positions, band diagrams of M-SAPCs and pristine PCN can be presented as shown in Figure 2B. The introduction of isolated metal ions resulted in a more positive conduction band minimum, indicating that intermediate band may be introduced by single metallic sites.

Being specific, the introduction of Fe^{2+} and Fe^{3+}, Co^{2+}, Ni^{2+}, In^{3+} and Sn^{4+} sites respectively shifted the CBM of the as-prepared catalyst for +0.28 eV, +0.21 eV, +0.19 eV, +0.09 eV and 0.24 eV. Based on the characterization details shown above, we can confirm that the metal ions were isolated by the nitrogen atoms of PCN skeleton with a little influence on the CBM. However, it is difficult to obtain the rigorous coordination status of isolated metal ions and N atoms since there are several possible structures of polymeric carbon nitrides prepared by thermal polymerization [38, 39]. In this case, a detailed theoretical simulation of M-SAPCs is necessary to reveal the comprehensive influences of isolated metal sites on the electronic configuration, thus leading to a further validation the structure of isolated metallic sites and a deep understanding of the changes in charge separation properties of M-SAPCs.

3.2 Development and validation of cluster models

Here is Figure 3.

Transition metals such as Fe, Cu, Zn, and Ni, and so forth have been used to construct models of single catalytic sites [34]. Based on previous experimental and theoretical results [34, 39], the skeleton of PCN can formed pores filled with six nitrogen lone-pairs of electrons in 2D planes, which is favorable ion coordination [39]. Additionally, the PCN prepared by thermal polymerization at high temperature showed the existence of $-NH_2$ as revealed in deconvoluted peak at 401.0 eV (Figure 1H). Previous reports showed that the mass ratio of the H element in PCN prepared by a thermal polymerization strategy is above 1.0% or more, quite close to that of poly(aminoimino)heptazine, i.e., melon (the hydrogen content of melon is approximately 1.5wt%) [38]. These facts suggest that melon could also exist in the M-SAPC matrix. In this case, two cluster models of Melem_3 (Figure 3A, left; Figure S9A) and Melem_4 (Figure 3A, Right; Figure S9B) [47] were built to represent the non-defected g-C_3N_4 units and melon units in the material matrix, respectively. Metal ions are coordinated by N atoms of Melem_3 and Melem_4 form single atomic sites. Distinguished by the geometry position of the metal ions, three models that represent single-atom photocatalysts could be built as well. It should be noted that the introduction

of cations usually results in localized charge sites in the PCN matrix. In this case, the charges and multiplicities of cluster models were set by referring to the chemical states of incorporated metals. Aiming to assess the stability of M-SAPCs, the formation energies of metal ions embedded in the Melem_3 and Melem_4 models were calculated. As shown in Figure 3B, all of the values of formation energy are negative, suggesting that the coordination of metal ions with nitrogen is thermodynamically favorable. These results indicate that both g-C_3N_4 units and melon units could stabilize metal ions by forming strong metal-nitrogen bonds.

The energy difference between the ionization potential (IP) and electron affinity (EA) usually corresponds to the band gap of material. Thus, the band gap is equivalent to, at the material level, the molecular fundamental gap. In this case, the fundamental gap usually approximately corresponds to the HOMO–LUMO gap [48]. In this work, wb97xd—a function with large amounts of Hartree–Fock (HF) exchange—was used to simulate the charge transfer densities during the excitation. Previous works revealed that this function usually overestimates the HOMO-LUMO gap and excitation energies in the case of p-conjugated polymers. Additionally, p-conjugated molecules adjacent to the one carrying a charge do strongly polarize (about 2 eV) in the solid state [48]. Although the computed HOMO-LUMO gap is considerably larger than the experimentally measured band gap, the relative changing tendencies of HOMO-LUMO gaps can still reveal the influence of ion incorporation if the same function and basis are used. In this case, the energetic levels of HOMO and LUMO of Melem_3, Melem_4, Melem_3M, Melem_4MC, and Melem_4MS were symmetrically investigated (Table S2) to reveal the influence of metal ions on the electronic configurations combined with density of states analysis, thus to validate the clusters models by estimating the correlations with experimental results.

Melem_3 and Melem_4 show similar HOMO and LUMO positions with similar HOMO-LUMO gaps of 7.61 eV and 7.73 eV, respectively, indicating that both the g-C_3N_4 units and melon units in the PCN matrix have similar electronic configurations. The N 2p states and C 2p states contribute to HOMO~HOMO-4 and LUMO~LUMO+4, respectively, indicating that N 2p states and C 2p states fundamentally compose the VB and CB of pristine PCN.

The introduction of metal ions into g-C_3N_4 units (Melem_3M) have almost no effect on the orbital composition of HOMO~HOMO-4, which is in accordance with the almost constant VBMs of M-SAPCs (Figure S4). The introducing the metal ions result in several intermediate energy levels which is 0.5 ~ 2 eV lower than the lowest energy level dominated by C 2p state (The amplified DOS curves of incorporated metals are inserted in the Figure 3C-H). Most of newly formed energetic levels compose LUMO levels, leading to narrowed HOMO-LUMO gaps (Figure 3C-H) compared with that of Melem_3 (Figure S10), which is in accordance with the experimental results (Figure 2B). On the other hand, the HOMO levels of Melem_4MS (Figure S11) and Melem_4MC (Figure S12) are significantly shifted after the introduction of metallic ions, due to the formations of new energetic levels composed by N 2p or M 3d states. Additionally, several intermediate energetic levels also appeared between the HOMO of Melem_4MS and that of Melem_4MC (These energy levels all formed LUMO of Melem_4M.), leading to a significantly narrowed HOMO-LUMO gap that is even smaller than the experimental band gap. The normalized LUMOs of Melem_3M, Melem_4MS and Melem_4MC (M being Co2+, Ni2+, In3+, and Sn4+) are summarized in Figure S13. The experimental CBMs of M-SAPCs and pristine PCN (black line) were also summarized for comparison. The changing tendency of LUMOs in the simulation results indicates that only the metal ions isolated by Melem_3 units (red line) show acceptable in accordance with M-SAPCs in terms of HOMO-LUMO positions for theoretical simulation and band positions for experimental results (The interrelationship between the HOMO-LUMO gap is explained in the beginning of this section). In this case, although the coordination of metal ions with melon units is thermodynamically acceptable, the band structures and electronic configurations show poor relationships with experimental band diagram. Therefore, cluster models of Melem_3M were utilized for simulating the influence of isolated metal sites on the excitation properties of M-SAPCs.

3.3 Molecular orbitals and transition densities

Here is Figure 4.

Visible light irradiation is used for photocatalytic H_2O_2 since UV irradiation (λ < 400 nm) will drastically decompose H_2O_2 generated by $2e^-$ ORR [10, 49]. In case of PCN and its derives, the adsorption edge is near 450~470 nm, i. e., the excitations with low energy play crucial roles in the visible light-driven H_2O_2 production [49]. In this case, the lowest-lying electronic transition computed by TDDFT usually represents the most possible excitations which can generate the electron hole pairs for photocatalytic $2e^-$ ORRs when using PCN and its derivatives [49]. In this work, the first 5 excited states (ES1-ES5, ES1 referring to the excited state 1 with the lowest excitation energy) of Melem_3 and Melem_3M were computed to investigate the most possible excitation properties and electronic transition properties [45]. The excitation energies of ES1 to ES5 are summarized in Figure S14. The computed optimal gap of Melem_3 is slightly larger than the experimental band gap, due to the fact that wb97xd contains a large amount of HF exchange. Therefore, the changing tendency of excitation energy was compared with the changing tendency of HOMO-LUMO gap, which is used to give an approximation for E_{fund}, leading to a primary understanding of the electron-hole pair binding energy (E_b, E_b is rigorously defined as: $E_b = E_{fund} - E_{opt,}$ in which E_{opt} is the energy difference between ES0 and ES1.) In this work, the approximated binding energy of electron-hole pairs (E_{abX}) in each excited state is defined as follows:

$$E_{abX} = E_{HOMO-LUMO} - E_{ecX}$$

where E_{abX} and E_{ecX} refer to the approximated binding energy of electron-hole pairs and the excitation energy of excited state No. X, respectively (Figure 3A). The E_{abX} values of Melem_3 and Melem_3M are shown as in Figure 3B. With the incorporation of Fe^{2+}, Fe^{3+}, Co^{2+} and Ni^{2+}, E_{abX} of Melem_3M significantly increased. On the other hand, Melem_3In3+ and Melem_3Sn4+ showed similar values of E_{abX}, which are both smaller than E_{abX} of Melem_3. These results indicate that the charge recombination may be suppressed by the introduction of In^{3+} and Sn^{4+} into g-C_3N_4 units, whereas the incorporation of Fe^{2+}, Fe^{3+}, Co^{2+}, and Ni^{2+} could result in a thermodynamically recombination tendency.

The distribution heatmaps of photo-generated electrons and holes (electronic transition densities) of Melem_3M were further investigated to identify the excitation types and to predict the spatial charge separation of the M-SAPCs. As shown in Figure S15 and

Figure S16, the distribution of electrons and holes at the first 5 ESs for Melem_3Fe2+, Fe3+, Co2+, and Ni2+ is extremely localized. Both the electrons and holes are distributed in a very small region just near the metal sites, indicating that typical localized transitions occurred. On the other hand, the lowest energy transitions (ES1-ES5) in Melem_3In3+ and Melem_3Sn4+ are dominated by charge transfer excitations, which are mostly associated with In and Sn atoms (Figure S17). To quantitatively investigate the charge separation properties of Melem_3M, the D index (i. e., the distance between the two barycenters of electrons or holes) and the Coulomb attraction between holes and electrons (E_{Coulmb}, also called exciton binding energy) were further computed (Figure 5G-H). D index and E_{Coulmb} of melem_3 were also computed for comparison. As given in Figure 5G-H, the transition distance of electron-hole pairs in Melem_3In3+ and Melem_3In4+ drastically increased compared with that in Melem_3 and considerably larger than most of the D index values of Melem_3Fe2+, Fe3+, Co2+, and Ni2+. E_{Coulmb} values of Melem_3In3+ and Melem_3In4+ were almost same as that in Melem_3, while E_{Coulmb} values of Melem_3Fe2+, Fe3+, Co2+, and Ni2+ drastically increased. There results further verified the charge separation tendency revealed by E_{abX}, further suggesting that charge separation of atomically dispersed In and Sn sites can significantly facilitate charge separation and suppress charge recombination. Note that 60%~70% of the electronic densities are concentrated at In sites, while only 40%~50% of the electrons are accumulated at Sn sites. Thus, with the help of obvious differences among the E_{abX}, D index, and E_{Coulmb} values of Melem_3 and Melem_3M, the highly concentrated electrons in Melem_3In3+ and Melem_3Sn4+ predict a much higher charge separation efficiency of In-SAPC and Sn-SAPC than that of Fe-SAPC, Co-SAPC and Ni-SAPC.

Here is Figure 6.

To further determine the influence of metal atoms on photo-redox reactions, the contribution of molecular orbitals (MOs) to holes and electrons from ES1 to ES5 of Melem_3M were investigated (Tables S3-4). Several MOs with energetic levels equal to or lower than the HOMO all contribute to holes (ranging from 0% to ~60%), while the LUMO is dominants for electron in ES1-ES3 of Melem_3In3+ and in ES1-ES5 of Melem_3Sn4+

(> 90%). These observations suggest that the electronic configuration of LUMO can almost represent the photogenerated electronic configuration if the electrons are accumulated to the atomic sites. Thus, the iso-surface of LUMO of Melem_In3+ and Melem_3Sn4+ was plotted as shown in Figures 6A-B. If can be clearly seen that electrons are concentrated at the In and Sn sites. The photo-generated electrons tend to form a highly condensed region atomic sites of In and Sn. The iso-surface of LUMO also showed that the electrons tend to form a highly condensed region in In sites during the excitation. Furthermore, the iso-surface of Melem_3In3+ and Melem_3Sn4+ showed an ideal electronic configuration for the adsorption of electrophilic oxygen, indicating that the ORR reduction could be accelerated at In and Sn sites (Figures 6C-D).

3.4 Experimental charge separation properties and activity for H_2O_2 production

Here is Figure 7.

To verify the theoretical prediction of charge separation efficiency obtained from the simulation of molecular orbitals and transition densities, the photochemical properties of as-prepared M-SAPCs were measured. As shown in the photoluminescence (PL) spectra (Figure 7A), the PL intensities of Sn-SAPC and In-SAPC were significantly decreased, indicating drastically suppressed charge recombination. On the other hand, the PL intensities of Fe-SAPC, Co-SAPC and Ni-SAPC all increased obviously, manifesting that the introduction of Fe, Co, and Ni ions into the PCN matrix facilitates charge recombination. The PL intensity ($I_{M\text{-}SAPC}$) of M-SAPC follows a sequence of $I_{Co} > I_{Fe} > I_{Ni} > I_{Sn} > I_{In}$, being in accordance with the E_{abx} ($E_{abCo} \approx E_{abNi} > E_{abSn} \approx E_{abIn}$) as shown in Figure 2. As shown in Nyquist plots, the diameter of the semicircle (In-SAPC) was the smallest (Figure 7B), indicating that In-SAPC showed the best charge transfer. Moreover, photocurrent (I_{ph}) measurements of the samples showed a significant increase in I_{ph} of In-SAPC and Sn-SAPC (Figure 7C), indicating enhanced efficiency of charge separation. On the other hand, the incorporation of Fe, Co, and Ni ions weakened I_{ph}, indicating significantly promoted charge recombination. The photocatalytic activity for H_2O_2 production (λ > 420 nm) of pristine PCN and as-prepared M-SAPC samples were measured with 10% (v/v) ethanol as

an electron donor. After 3 reproductive experiments (Figure 7D and Figure S18), In-SAPC and Sn-SAPC showed superior photocatalytic activity among all of the M-SAPC samples, while the atomically dispersed Fe, Co, and Ni sites all drastically decreased the photocatalytic activity compared with that of pristine PCN, which is consisted with both experimental and theoretical charge separation properties. The performance of the In-SAPC remained >90% after 5 repetitive photocatalytic reactions (Figure S19). After 5 reaction circles, the crystallinity of In-SAPC showed no obvious change (Figure S20A), and the chemical states of N, C and In kept almost constant (Figure S20B-D). These results indicate that the In-SAPC showed good stability during the photocatalytic activity. Note that the metal particle may also sever as co-catalyst during photocatalytic reactions. Thus, the activity of metal nanoparticle loaded PCN were also measured to investigate whether nanoparticle could contribute to photocatalytic H_2O_2 production. Since In-SAPC is the most efficient photocatalyst in this work, 3, 5, 10 mmol were mixed with melamine to prepare the In nanoparticle loaded PCN (Figure S21A-C). The photocatalytic H_2O_2 production significantly decreased (Figure S21D) with the addition of increasing amount of metal source ($InCl_3$). These results indicated that the remained In nanoparticles significantly suppressed the photocatalytic synthesis of photocatalytic activity. From the results above, experimental charge separation properties of M-SAPC showed good accordance with the computed charge transfer profile of Melem_3M. The correlations among activity and experimental and theoretical charge separation properties also manifested the rationalities of the proposed model and methodology for estimating charge separation properties.

4. Conclusion

In summary, a series of metal ion-incorporated single-atom photocatalyst (M-SAPCs) was prepared by isolating TM metal (Fe, Co, Ni) and main-group (In, Sn) sites with pyridinic N atoms in PCN skeleton. The chemical state of atomically dispersed Fe is between (II) and (III), and the chemical states of Co, Ni, In and Sn species catalyst is close (II), (II), (III) and (IV), respectively. The simulation results revealed that the metal ions isolated by non-defected Melem_3 units are consistent with the practically prepared M-SAPC in terms of

band structures and electronic configurations. E_{abX}, transition density distribution of elections and holes, D index and E_{Coulmb} revealed that the incorporation of atomically dispersed main-group metals (In (III) and Sn (IV)) significantly improved the charge separation efficiency. Additionally, the iso-surface of the dominant MO (electrons) in the models of Melem_3In3+ and Melem_3Sn4+ showed an ideal electronic configuration for the adsorption of electrophilic oxygen, indicating that the ORR reduction could be accelerated by In and Sn sites. Furthermore, the experimental charge separation properties of M-SAPCs showed good accordance with the computed charge transfer profile of Melem_3M. The correlations among activity and experimental and theoretical charge separation properties also showed the rationalities of the proposed model for estimating charge separation properties. Our work provides not only a theoretical guideline based on the validated electronic configuration and excitation properties but also a blueprint for the design of single-atom photocatalyst with a high charge separation profile at atomic levels. Combined with the traditional simulation strategies such as CHE models and transition states, a precise benchmark for predicting both activity and selectivity might be established for many artificial photo-synthesis systems in a very near future.

Acknowledgement

The authors acknowledge the financial support of Mitsubishi Chemical Corporation, JSPS Grant-in-Aid for Scientific Research (B, No. 20H02847), Grant-in-Aid for JSPS Fellows (DC2, 20J13064), Project National Natural Science Foundation of China (21805191, 21972094), the Guangdong Basic and Applied Basic Research Foundation (2020A151501982), Shenzhen Pengcheng Scholar Program, Shenzhen Peacock Plan (KQJSCX20170727100802505, KQTD2016053112042971). The authors thank Dr. Nan Jian from the Electron Microscope Center of the Shenzhen University for his help in HRTEM measurement.

Author Contribution

Zhenyuan Teng: Conceptualization, Methodology, Software, Formal analysis, Writing - original draft, Data curation. Wenan Cai: Investigation, Software, Formal analysis, Data curation. Wenwen Sim: Software, Formal analysis, Chengyin Wang: Writing - review & editing. Qitao Zhang: Conceptualization, Supervision, Software, Writing - review & editing. Chenliang Su: Writing - review & editing. Teruhisa Ohno: Conceptualization, Writing - review & editing, Funding acquisition, Data curation.

Declaration of Interests

The authors declare no competing financial interest.

References

[1] K.P. Bryliakov, Catalytic asymmetric oxygenations with the environmentally benign oxidants H_2O_2 and O_2, Chem. Rev., 117 (2017) 11406-11459. https://doi.org/10.1021/acs.chemrev.7b00167.

[2] S.J. Freakley, Q. He, J.H. Harrhy, L. Lu, D.A. Crole, D.J. Morgan, E.N. Ntainjua, J.K. Edwards, A.F. Carley, A.Y. Borisevich, C.J. Kiely, G.J. Hutchings, Palladium-tin catalysts for the direct synthesis of H_2O_2 with high selectivity, Science, 351 (2016) 965-968. https://doi.org/10.1126/science.aad5705.

[3] H.B. Gray, Powering the planet with solar fuel, Nat. Chem., 1 (2009) 7-7. https://doi.org/10.1038/nchem.141.

[4] S.A. Mousavi Shaegh, N.-T. Nguyen, S.M. Mousavi Ehteshami, S.H. Chan, A membraneless hydrogen peroxide fuel cell using Prussian Blue as cathode material, Energy Environ. Sci., 5 (2012) 8225-8228. https://doi.org/10.1039/C2EE21806B.

[5] S. Yang, A. Verdaguer-Casadevall, L. Arnarson, L. Silvioli, V. Čolić, R. Frydendal, J. Rossmeisl, I. Chorkendorff, I.E.L. Stephens, Toward the decentralized electrochemical production of H_2O_2: A focus on the catalysis, ACS Catal., 8 (2018) 4064-4081. https://doi.org/10.1021/acscatal.8b00217.

[6] Y. Yi, L. Wang, G. Li, H. Guo, A review on research progress in the direct synthesis of hydrogen peroxide from hydrogen and oxygen: Noble-metal catalytic method, fuel-cell method and plasma method, Catal. Sci. Technol., 6 (2016) 1593-1610. https://doi.org/10.1039/C5CY01567G.

[7] H. Hou, X. Zeng, X. Zhang, Production of hydrogen peroxide by photocatalytic processes, Angew. Chem. Int. Ed., n/a (2019). https://doi.org/10.1002/anie.201911609.

[8] X. Shi, S. Siahrostami, G.-L. Li, Y. Zhang, P. Chakthranont, F. Studt, T.F. Jaramillo, X. Zheng, J.K. Nørskov, Understanding activity trends in electrochemical water oxidation to form hydrogen peroxide, Nat. Commun., 8 (2017) 701. https://doi.org/10.1038/s41467-017-00585-6.

[9] Z. Teng, W. Cai, S. Liu, C. Wang, Q. Zhang, C. Su, T. Ohno, Bandgap engineering of polymetric carbon nitride copolymerized by 2,5,8-triamino-tri-s-triazine (melem) and barbituric acid for efficient nonsacrificial photocatalytic H_2O_2 production, Appl. Catal. B: Environ., 271 (2020) 118917. https://doi.org/10.1016/j.apcatb.2020.118917.

[10] Y. Shiraishi, S. Kanazawa, Y. Kofuji, H. Sakamoto, S. Ichikawa, S. Tanaka, T. Hirai, Sunlight-driven hydrogen peroxide production from water and molecular oxygen by metal-free photocatalysts, Angew. Chem. Int. Ed., 53 (2014) 13454-13459. https://doi.org/10.1002/anie.201407938.
[11] K. Fuku, K. Sayama, Efficient oxidative hydrogen peroxide production and accumulation in photoelectrochemical water splitting using a tungsten trioxide/bismuth vanadate photoanode, Chem. Commun., 52 (2016) 5406-5409. https://doi.org/10.1039/C6CC01605G.
[12] J.H. Baek, T.M. Gill, H. Abroshan, S. Park, X. Shi, J. Nørskov, H.S. Jung, S. Siahrostami, X. Zheng, Selective and efficient Gd-doped $BiVO_4$ photoanode for two-electron water oxidation to H_2O_2, ACS Energy Lett., 4 (2019) 720-728. https://doi.org/10.1021/acsenergylett.9b00277.
[13] C. Chu, Q. Zhu, Z. Pan, S. Gupta, D. Huang, Y. Du, S. Weon, Y. Wu, C. Muhich, E. Stavitski, K. Domen, J.-H. Kim, Spatially separating redox centers on 2D carbon nitride with cobalt single atom for photocatalytic H_2O_2 production, PNAS, 117 (2020) 6376-6382. https://doi.org/10.1073/pnas.1913403117.
[14] W. Fan, B. Zhang, X. Wang, W. Ma, D. Li, Z. Wang, M. Dupuis, J. Shi, S. Liao, C. Li, Efficient hydrogen peroxide synthesis by metal-free polyterthiophene via photoelectrocatalytic dioxygen reduction, Energy Environ. Sci., 13 (2020) 238-245. https://doi.org/10.1039/C9EE02247C.
[15] M. Jakešová, D.H. Apaydin, M. Sytnyk, K. Oppelt, W. Heiss, N.S. Sariciftci, E.D. Głowacki, Hydrogen-bonded organic semiconductors as stable photoelectrocatalysts for efficient hydrogen peroxide photosynthesis, Adv. Funct. Mater., 26 (2016) 5248-5254. https://doi.org/10.1002/adfm.201601946.
[16] Y. Shiraishi, T. Takii, T. Hagi, S. Mori, Y. Kofuji, Y. Kitagawa, S. Tanaka, S. Ichikawa, T. Hirai, Resorcinol–formaldehyde resins as metal-free semiconductor photocatalysts for solar-to-hydrogen peroxide energy conversion, Nat. Mater., 18 (2019) 985-993. https://doi.org/10.1038/s41563-019-0398-0.
[17] Z. Wei, M. Liu, Z. Zhang, W. Yao, H. Tan, Y. Zhu, Efficient visible-light-driven selective oxygen reduction to hydrogen peroxide by oxygen-enriched graphitic carbon nitride polymers, Energy Environ. Sci., 11 (2018) 2581-2589. https://doi.org/10.1039/C8EE01316K.
[18] M. Teranishi, S.-i. Naya, H. Tada, In situ liquid phase synthesis of hydrogen peroxide from molecular oxygen using gold nanoparticle-loaded titanium(IV) dioxide photocatalyst, J. Am. Chem. Soc., 132 (2010) 7850-7851. https://doi.org/10.1021/ja102651g.
[19] A.J. Hoffman, E.R. Carraway, M.R. Hoffmann, Photocatalytic production of H_2O_2 and organic peroxides on quantum-sized semiconductor colloids, Environ. Sci. Technol., 28 (1994) 776-785. https://doi.org/10.1021/es00054a006.
[20] H.-i. Kim, O.S. Kwon, S. Kim, W. Choi, J.-H. Kim, Harnessing low energy photons (635 nm) for the production of H_2O_2 using upconversion nanohybrid photocatalysts, Energy Environ. Sci., 9 (2016) 1063-1073. https://doi.org/10.1039/C5EE03115J.
[21] A. Kulkarni, S. Siahrostami, A. Patel, J.K. Nørskov, Understanding catalytic activity trends in the oxygen reduction reaction, Chem. Rev., 118 (2018) 2302-2312. https://doi.org/10.1021/acs.chemrev.7b00488.
[22] E. Watanabe, H. Ushiyama, K. Yamashita, Theoretical studies on the mechanism of oxygen reduction reaction on clean and O-substituted Ta_3N_5(100) surfaces, Catal. Sci. Technol., 5 (2015) 2769-2776. https://doi.org/10.1039/C5CY00088B.

[23] C. Chu, D. Huang, Q. Zhu, E. Stavitski, J.A. Spies, Z. Pan, J. Mao, H.L. Xin, C.A. Schmuttenmaer, S. Hu, J.-H. Kim, Electronic tuning of metal nanoparticles for highly efficient photocatalytic hydrogen peroxide production, ACS Catal., 9 (2019) 626-631. https://doi.org/10.1021/acscatal.8b03738.

[24] M.M. Montemore, M.A. Van Spronsen, R.J. Madix, C.M. Friend, O_2 activation by metal surfaces: Implications for bonding and reactivity on heterogeneous catalysts, Chem. Rev., 118 (2018) 2816-2862. https://doi.org/10.1021/acs.chemrev.7b00217.

[25] M.L. Pegis, C.F. Wise, D.J. Martin, J.M. Mayer, Oxygen reduction by homogeneous molecular catalysts and electrocatalysts, Chem. Rev., 118 (2018) 2340-2391. https://doi.org/10.1021/acs.chemrev.7b00542.

[26] A. Wang, J. Li, T. Zhang, Heterogeneous single-atom catalysis, Nat. Rev. Chem., 2 (2018) 65-81. https://doi.org/10.1038/s41570-018-0010-1.

[27] R. Shen, W. Chen, Q. Peng, S. Lu, L. Zheng, X. Cao, Y. Wang, W. Zhu, J. Zhang, Z. Zhuang, C. Chen, D. Wang, Y. Li, High-concentration single atomic Pt sites on hollow CuS_x for selective O_2 reduction to H_2O_2 in acid solution, Chem, 5 (2019) 2099-2110. https://doi.org/10.1016/j.chempr.2019.04.024.

[28] S. Yang, J. Kim, Y.J. Tak, A. Soon, H. Lee, Single-atom catalyst of platinum supported on titanium nitride for selective electrochemical reactions, Angew. Chem. Int. Ed., 55 (2016) 2058-2062. https://doi.org/10.1002/anie.201509241.

[29] J. Gao, H.b. Yang, X. Huang, S.-F. Hung, W. Cai, C. Jia, S. Miao, H.M. Chen, X. Yang, Y. Huang, T. Zhang, B. Liu, Enabling direct H_2O_2 production in acidic media through rational design of transition metal single atom catalyst, Chem, 6 (2020) 658-674. https://doi.org/10.1016/j.chempr.2019.12.008.

[30] E. Jung, H. Shin, B.-H. Lee, V. Efremov, S. Lee, H.S. Lee, J. Kim, W. Hooch Antink, S. Park, K.-S. Lee, S.-P. Cho, J.S. Yoo, Y.-E. Sung, T. Hyeon, Atomic-level tuning of Co–N–C catalyst for high-performance electrochemical H_2O_2 production, Nat. Mater., 19 (2020) 436-442. https://doi.org/10.1038/s41563-019-0571-5.

[31] J.K. Nørskov, J. Rossmeisl, A. Logadottir, L. Lindqvist, J.R. Kitchin, T. Bligaard, H. Jónsson, Origin of the overpotential for oxygen reduction at a fuel-cell cathode, J. Phys. Chem. B, 108 (2004) 17886-17892. https://doi.org/10.1021/jp047349j.

[32] T. Takata, K. Domen, Particulate photocatalysts for water splitting: Recent advances and future prospects, ACS Energy Lett., 4 (2019) 542-549. https://doi.org/10.1021/acsenergylett.8b02209.

[33] T. Takata, J. Jiang, Y. Sakata, M. Nakabayashi, N. Shibata, V. Nandal, K. Seki, T. Hisatomi, K. Domen, Photocatalytic water splitting with a quantum efficiency of almost unity, Nature, 581 (2020) 411-414. https://doi.org/10.1038/s41586-020-2278-9.

[34] X. Chen, H. Rui, DFT-based study of single transition metal atom doped g-C_3N_4 as alternative oxygen reduction reaction catalysts, Int. J. Hydrog. Energy, 44 (2019) 15409-15416. https://doi.org/10.1016/j.ijhydene.2019.04.057.

[35] Y. Nosaka, A. Nosaka, Introduction to photocatalysis: From basic science to applications, (2016) ISBN: 978-971-78262-78320-78265.

[36] Y. Inoue, Photocatalytic water splitting by RuO_2-loaded metal oxides and nitrides with d^0- and d^{10} -related electronic configurations, Energy Environ. Sci., 2 (2009) 364-386. https://doi.org/10.1039/B816677N.

[37] C. Adamo, D. Jacquemin, The calculations of excited-state properties with time-dependent density functional theory, Chem. Soc. Rev., 42 (2013) 845-856. https://doi.org/10.1039/C2CS35394F.
[38] F.K. Kessler, Y. Zheng, D. Schwarz, C. Merschjann, W. Schnick, X. Wang, M.J. Bojdys, Functional carbon nitride materials — design strategies for electrochemical devices, Nat. Rev. Mater., 2 (2017) 17030. https://doi.org/10.1038/natrevmats.2017.30.
[39] W.J. Ong, L.L. Tan, Y.H. Ng, S.T. Yong, S.P. Chai, Graphitic carbon nitride ($g\text{-}C_3N_4$)-based photocatalysts for artificial photosynthesis and environmental remediation: Are we a step closer to achieving sustainability?, Chem. Rev., 116 (2016) 7159-7329. https://doi.org/10.1021/acs.chemrev.6b00075.
[40] B. Zhu, P. Xia, W. Ho, J. Yu, Isoelectric point and adsorption activity of porous $g\text{-}C_3N_4$, Appl. Surf. Sci., 344 (2015) 188-195. https://doi.org/10.1016/j.apsusc.2015.03.086.
[41] L. Zuccaro, J. Krieg, A. Desideri, K. Kern, K. Balasubramanian, Tuning the isoelectric point of graphene by electrochemical functionalization, Sci. Rep., 5 (2015) 11794. https://doi.org/10.1038/srep11794.
[42] L. Tian, F. Chen, Multiwfn: A multifunctional wavefunction analyzer, J. Comput. Chem., 33 (2012) 580-592. https://doi.org/10.1002/jcc.22885.
[43] S. Kraner, R. Scholz, F. Plasser, C. Koerner, K. Leo, Exciton size and binding energy limitations in one-dimensional organic materials, J. Phys. Chem., 143 (2015) 244905. https://doi.org/10.1063/1.4938527.
[44] S. Kraner, G. Prampolini, G. Cuniberti, Exciton binding energy in molecular triads, J. Phys. Chem. C, 121 (2017) 17088-17095. https://doi.org/10.1021/acs.jpcc.7b03923.
[45] X. Li, W. Bi, L. Zhang, S. Tao, W. Chu, Q. Zhang, Y. Luo, C. Wu, Y. Xie, Single-atom Pt as Co-catalyst for enhanced photocatalytic H_2 evolution, Adv. Mater., 28 (2016) 2427-2431. https://doi.org/10.1002/adma.201505281.
[46] A.V. Naumkin, A. Kraut-Vass, S.W. Gaarenstroom, C.J. Powell, NIST X-ray Photoelectron Spectroscopy Database, (2012). http://dx.doi.org/10.18434/T4T88K.
[47] V.W.-h. Lau, I. Moudrakovski, T. Botari, S. Weinberger, M.B. Mesch, V. Duppel, J. Senker, V. Blum, B.V. Lotsch, Rational design of carbon nitride photocatalysts by identification of cyanamide defects as catalytically relevant sites, Nat. Comm., 7 (2016) 12165. 10.1038/ncomms12165.
[48] J.-L. Bredas, Mind the gap!, Mater. Horiz., 1 (2014) 17-19. https://doi.org/10.1039/C3MH00098B.
[49] Y. Kofuji, S. Ohkita, Y. Shiraishi, H. Sakamoto, S. Tanaka, S. Ichikawa, T. Hirai, Graphitic carbon nitride doped with biphenyl diimide: Efficient photocatalyst for hydrogen peroxide production from water and molecular oxygen by sunlight, ACS Catal., 6 (2016) 7021-7029. https://doi.org/10.1021/acscatal.6b02367.

Scheme 1:

A

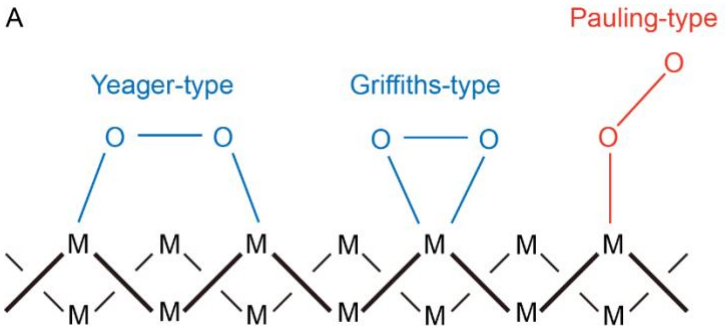
Yeager-type
Griffiths-type
Pauling-type
O
O
O
O
O
M
M
M
M
M
M
M
M
M
M
M
M
M
M

B

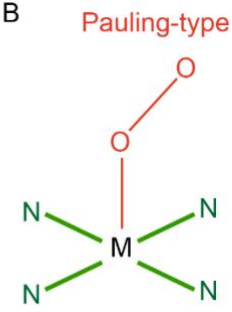
Pauling-type
O
O
N
N
M
N
N

1 Figure 1:

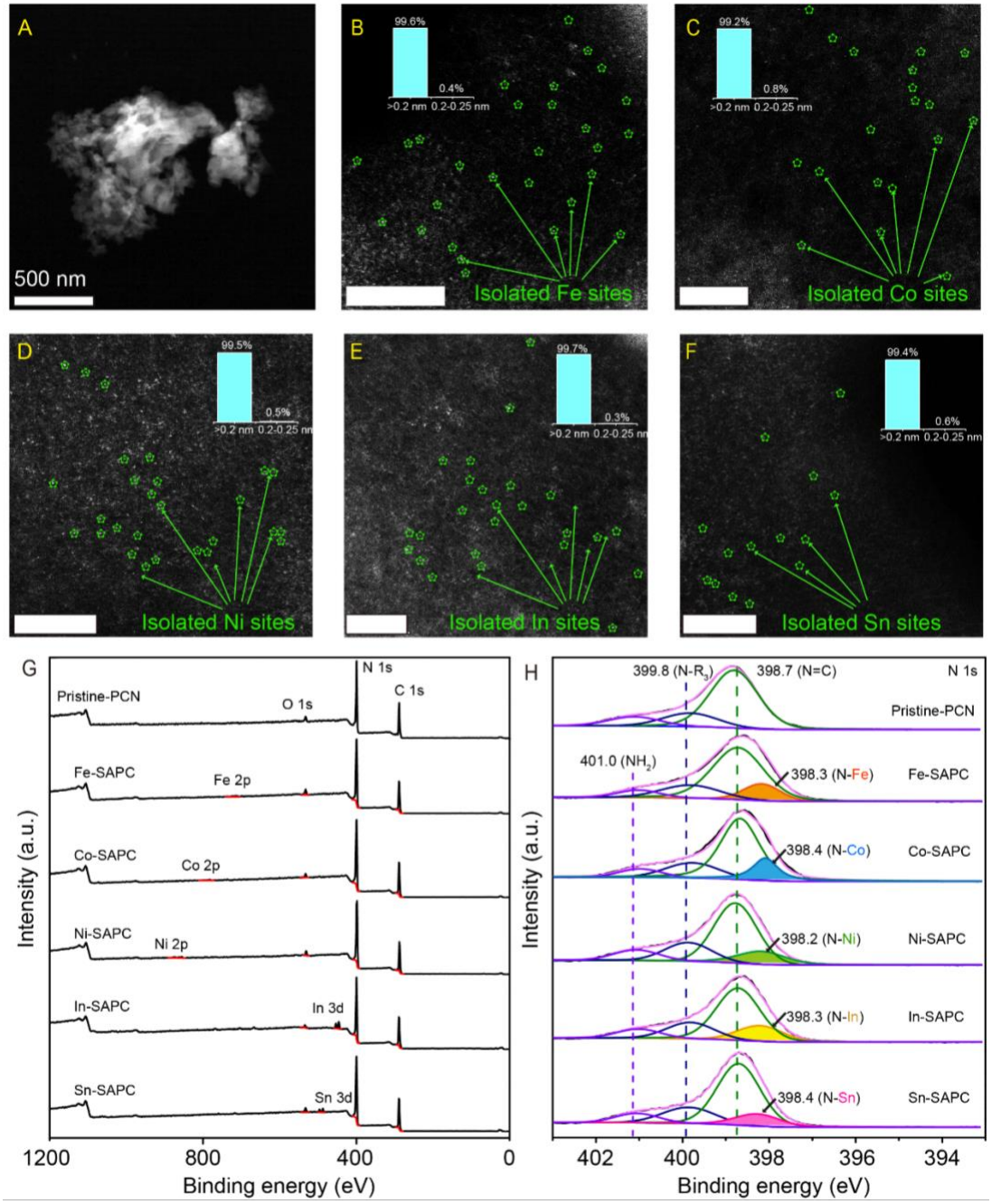
A
500 nm
B
99.6%
0.4%
>0.2 nm 0.2-0.25 nm
Isolated Fe sites
C
99.2%
0.8%
>0.2 nm 0.2-0.25 nm
Isolated Co sites
D
99.5%
0.5%
Isolated Ni sites
E
99.7%
0.3%
Isolated In sites
F
99.4%
0.6%
Isolated Sn sites
G
Pristine-PCN
O 1s
N 1s
C 1s
Fe-SAPC
Fe 2p
Co-SAPC
Co 2p
Ni-SAPC
Ni 2p
In-SAPC
In 3d
Sn-SAPC
Sn 3d
Intensity (a.u.)
1200
800
400
0
Binding energy (eV)
H
399.8 (N-R3)
398.7 (N=C)
N 1s
Pristine-PCN
401.0 (NH2)
398.3 (N-Fe)
Fe-SAPC
398.4 (N-Co)
Co-SAPC
398.2 (N-Ni)
Ni-SAPC
398.3 (N-In)
In-SAPC
398.4 (N-Sn)
Sn-SAPC
Intensity (a.u.)
402
400
398
396
394
Binding energy (eV)

2

3

Figure 2:

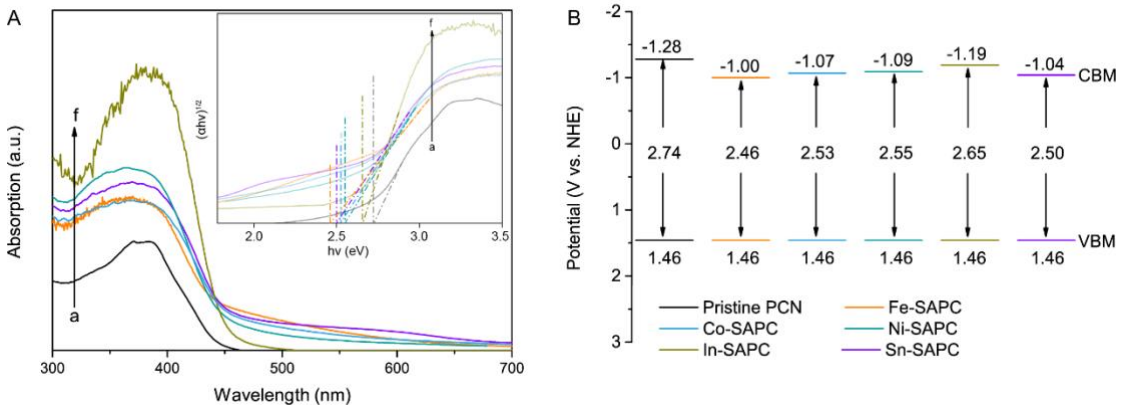
A
Absorption (a.u.)
Wavelength (nm)
300
400
500
600
700
f
a
(αhν)^1/2
hν (eV)
2.0
2.5
3.0
3.5
B
Potential (V vs. NHE)
-2
-1
0
1
2
3
-1.28
-1.00
-1.07
-1.09
-1.19
-1.04
CBM
2.74
2.46
2.53
2.55
2.65
2.50
1.46
1.46
1.46
1.46
1.46
1.46
VBM
Pristine PCN
Co-SAPC
In-SAPC
Fe-SAPC
Ni-SAPC
Sn-SAPC

Figure 3:

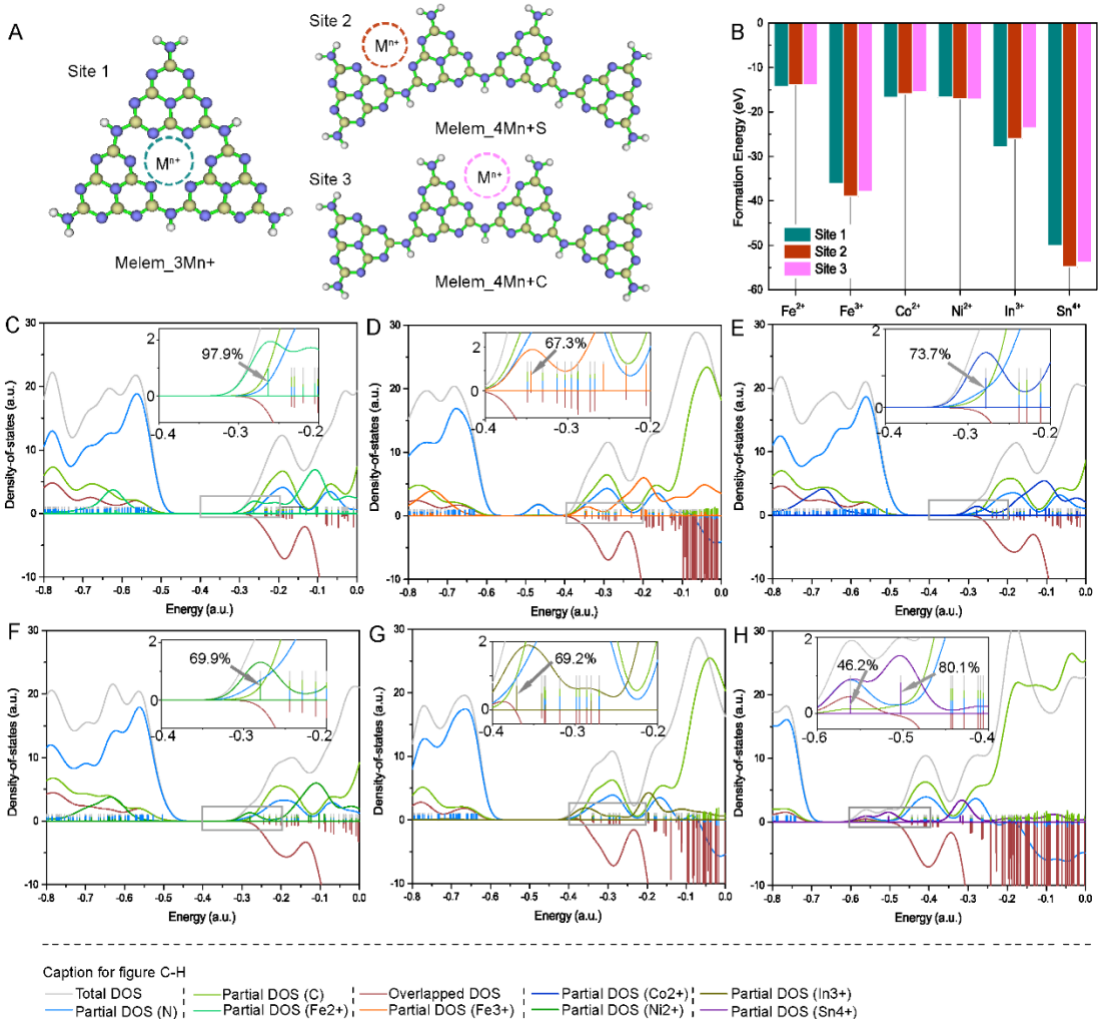

Caption for figure C-H

Total DOS
Partial DOS (N)
Partial DOS (C)
Partial DOS (Fe2+)
Overlapped DOS
Partial DOS (Fe3+)
Partial DOS (Co2+)
Partial DOS (Ni2+)
Partial DOS (In3+)
Partial DOS (Sn4+)

Figure 4:

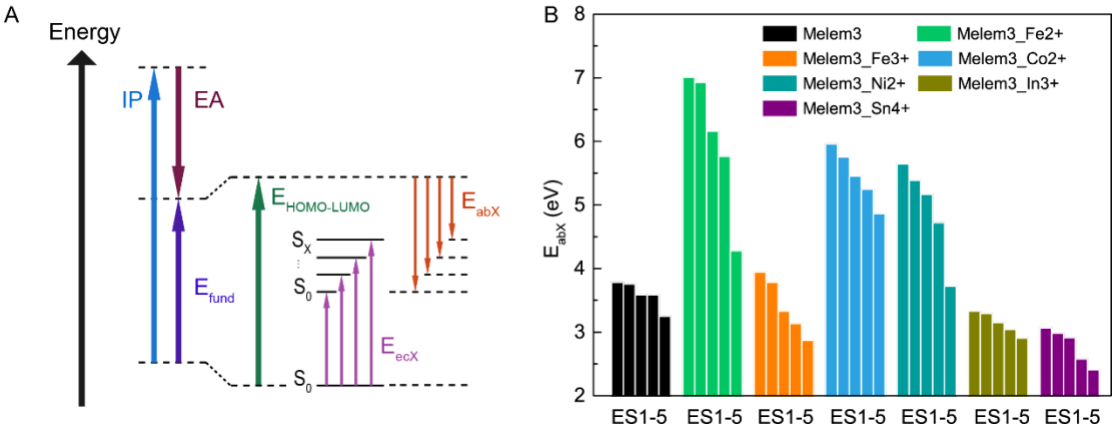
A
Energy
IP
EA
E_HOMO-LUMO
E_abX
E_fund
S_X
S_0
E_ecX
S_0
B
Melem3
Melem3_Fe2+
Melem3_Fe3+
Melem3_Co2+
Melem3_Ni2+
Melem3_In3+
Melem3_Sn4+
E_abX (eV)
8
7
6
5
4
3
2
ES1-5
ES1-5
ES1-5
ES1-5
ES1-5
ES1-5
ES1-5

Figure 5:

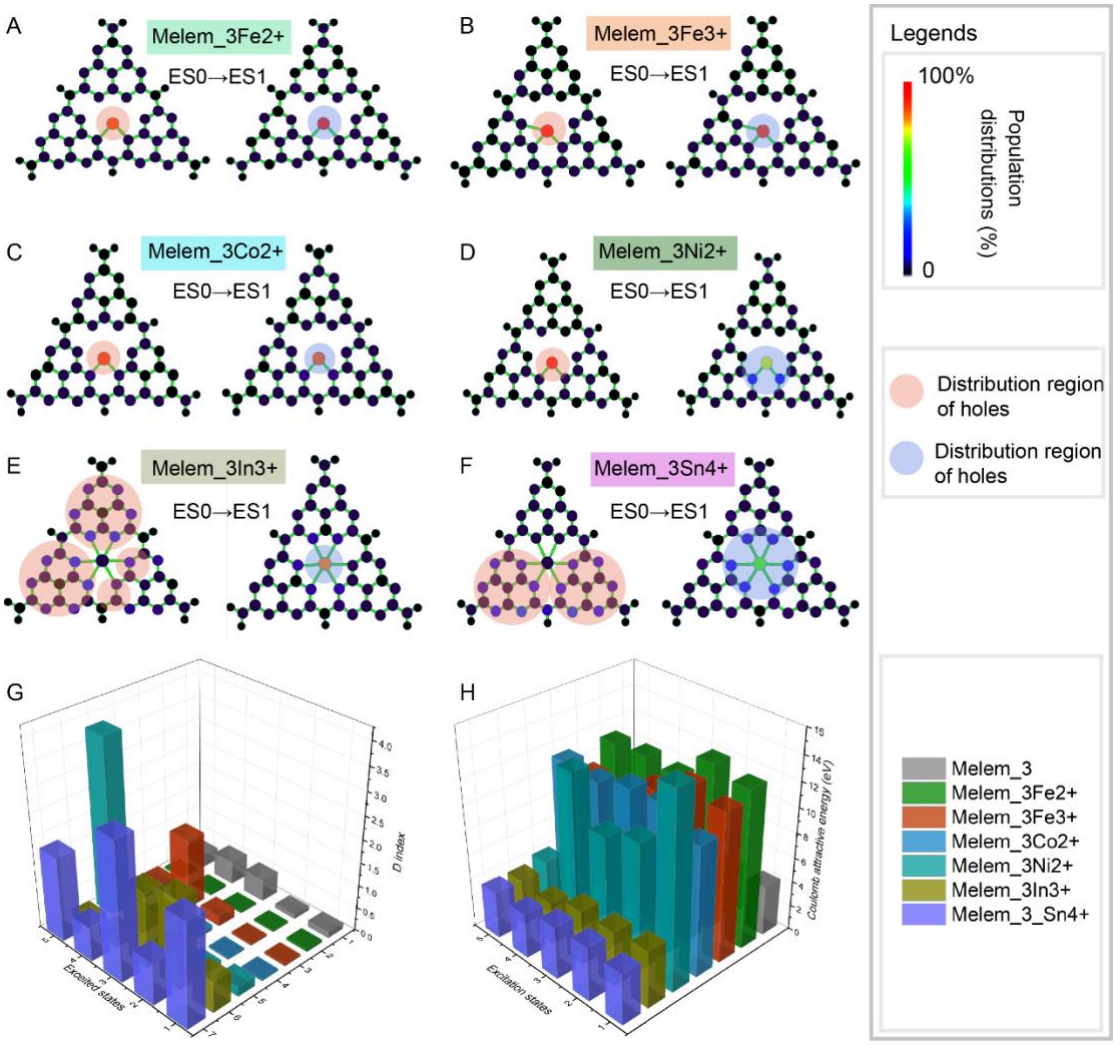
A
Melem_3Fe2+
ES0→ES1
B
Melem_3Fe3+
ES0→ES1
C
Melem_3Co2+
ES0→ES1
D
Melem_3Ni2+
ES0→ES1
E
Melem_3In3+
ES0→ES1
F
Melem_3Sn4+
ES0→ES1
G
D index
Excited states
H
Coulomb attractive energy (eV)
Excitation states
Legends
100%
0
Population distributions (%)
Distribution region of holes
Distribution region of holes
Melem_3
Melem_3Fe2+
Melem_3Fe3+
Melem_3Co2+
Melem_3Ni2+
Melem_3In3+
Melem_3_Sn4+

Figure 6:

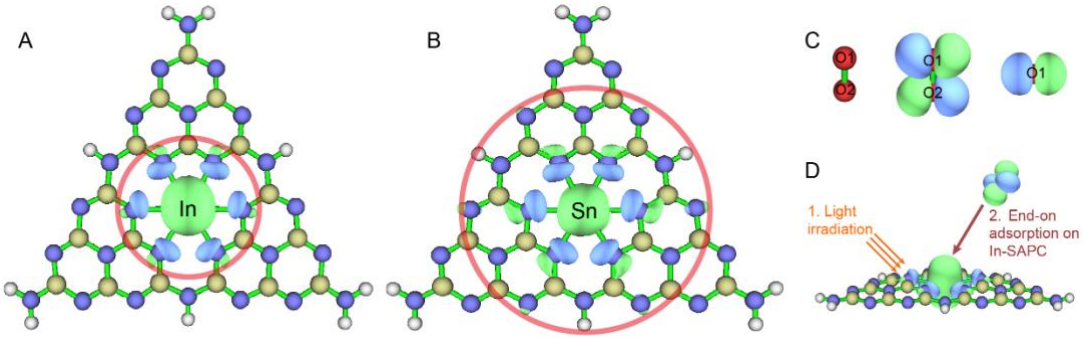
A
In
B
Sn
C
O1
O2
O1
O2
O1
D
1. Light irradiation
2. End-on adsorption on In-SAPC

Figure 7:

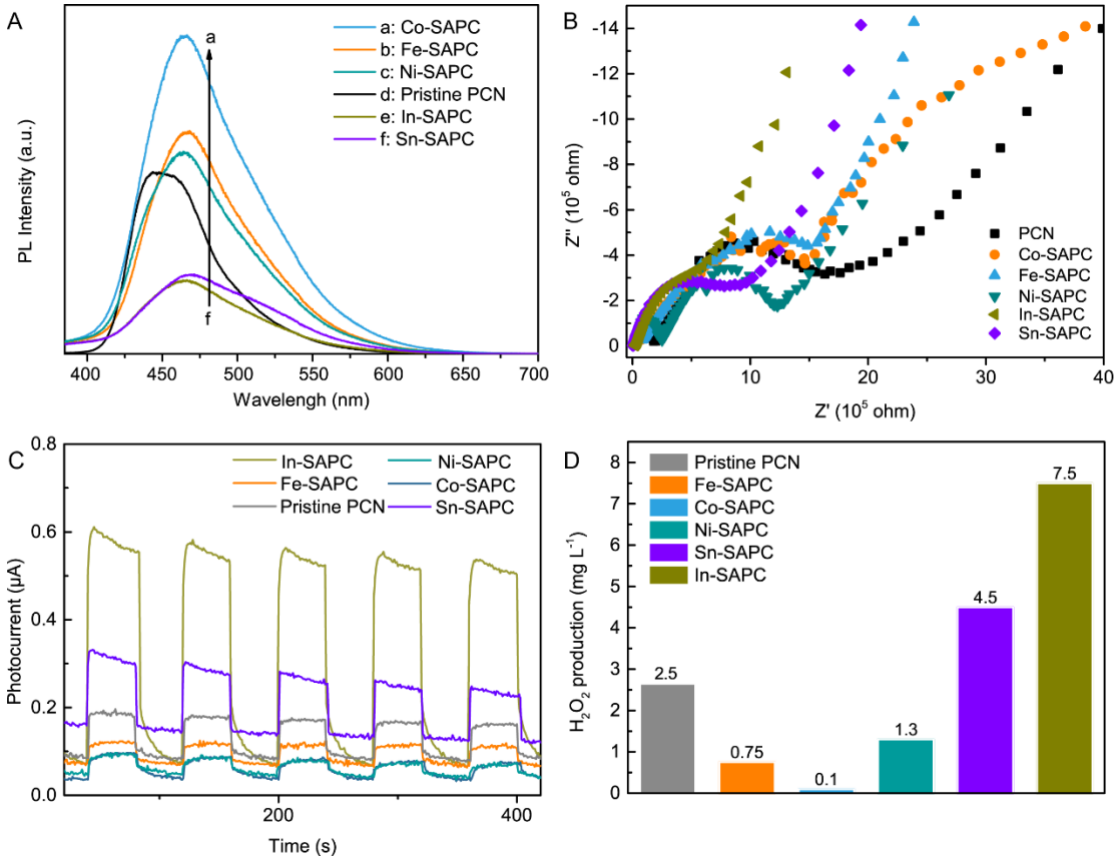
A
a: Co-SAPC
b: Fe-SAPC
c: Ni-SAPC
d: Pristine PCN
e: In-SAPC
f: Sn-SAPC
PL Intensity (a.u.)
Wavelengh (nm)
B
Z'' (10^5 ohm)
Z' (10^5 ohm)
PCN
Co-SAPC
Fe-SAPC
Ni-SAPC
In-SAPC
Sn-SAPC
C
In-SAPC
Ni-SAPC
Fe-SAPC
Co-SAPC
Pristine PCN
Sn-SAPC
Photocurrent (μA)
Time (s)
D
Pristine PCN
Fe-SAPC
Co-SAPC
Ni-SAPC
Sn-SAPC
In-SAPC
H_2O_2 production (mg L^{-1})
2.5
0.75
0.1
1.3
4.5
7.5

Captions

Scheme 1. Adsorption types of molecular oxygen on metallic surface. Molecular oxygen adsorption on the surface of (A) metal particles and (B) single atom catalyst.

Figure 1. Characterization of M-SAPCs. (A) Low-magnification HAADF-STEM image of pristine PCN. High-magnification HAADF-STEM images of (B) Fe-SAPC, (C) Co-SAPC, (D) Ni-SAPC, (E) In-SAPC and (F) Sn-SAPC. Inset is the size distribution of the bright spots. (G) XPS-survey spectra of pristine PCN and M-SAPCs. (H) High-resolution XPS N 1s spectra of pristine PCN and M-SAPCs.

Figure 2. Optical absorption and band positions of pristine PCN and M-SAPC samples. (A) UV-vis spectra of pristine PCN and M-SAPC samples: absorbance spectra with inserted Tauc plots. Lines a-f: a: pristine PCN; b: Fe-SAPC; c: Co-SAPC; d: Ni-SAPC; e: In-SAPC; c: Sn-SAPC. (B) Band diagrams of PCN and as-prepared M-SAPC samples.

Figure 3. Stabilities and electronic configurations of cluster models. (A) Schematic diagram for two cluster models and three possible sites for coordination of metal ions. (B) Formation energies of various transition metals embedded in Melem_3 or Melem_4. Computed simulation of density of states (DOS) with different embedded (C) Fe^{2+}, (D) Fe^{3+}, (E) Co^{2+}, (F) Ni^{2+}, (G) In^{3+}, and (H) Sn^{4+} with the coordination of the large nitrogen pots in Melem_3. The insert figures are amplified the states (metal) that formed the orbitals those close to LUMO.

Figure 4. Approximate binding energies of Melem_3 and Melem_3M. (A) Illustration of gap energies in the molecular case: S_0 denotes the electronic ground state and S_X is the No. X excited state. The $S_X \rightarrow S_0$ energy difference then corresponds to the excitation energy E_{ecX}. The magnitude of the ionization potential is shown by the blue-colored vertical line and the magnitude of the electron affinity is shown by the wine-colored vertical line; the IP→EA difference represents (violet line) the fundamental gap, E_{fund}, which is usually smaller than the HOMO-LUMO gap, $E_{HOMO\text{-}LUMO}$. The approximate electron–hole pair binding energy, E_{abX}, is given by $E_{HOMO\text{-}LUMO}$ - E_{ecX}. (B) The computed approximate binding energies of Melem_3 and Melem_3M for the five lowest-lying excited states.

Figure 5. Transition densities of Melem_3M. Population of electron and hole distributions (vertical excitation at the excited state 1) and quantitative investigation of the charge separation. The color in the heatmap refers to the sum of MO contribution at each atom for simulated electrons and holes of (A) Melem_3Fe2+, (B) Melem_3Fe3+, (C) Melem_3Co2+, (B) Melem_3Ni2+, (E) Melem_3In3+, and (F) Melem_3Sn4+ . The oringe and blue shadows are accumulated regions of hole and electrons, respectively. (G) D index and (H) Coulomb attraction between hole and electron of Melem_3 and Melem_3M.

Figure 6. Visualization of the dominant contributing molecular orbitals and transition. Visualization of the LUMOs of (A) Melem_3In3+ and (B) Melem_3Sn4+. Red circles refer to the observable region of isosurface on Melem_3In3+ and Melem_3Sn4+. (C)

Visualization of HOMO of O_2. (D) Schematic diagram of possible O_2 adsorption configuration on the Melem_3In3+ surface after light irradiation.

Figure 7. Photoexcitation properties and photocatalytic activities of pristine PCN and M-SAPCs. (A) Photoluminescence spectra of pristine PCN and M-SAPCs under 365 nm excitation. (B) EIS of electrodes prepared by PCN and M-SAPCs under visible light irradiation. (C) Photocurrents of electrodes prepared by PCN, PCNBA0.2 and PCNBA0.5. (line a: pristine PCN; line b: PCNBA0.2; line c: PCNBA0.2Co0.5%) (D) Photocatalytic activities of pristine PCN and M-SAPCs for H_2O_2 production in 10% (v/v) ethanol aqueous solution.